Hierarchical Assembly of Plasmonic Nanostructures Using Virus Capsid Scaffolds on DNA Origami Templates

Debin Wang,[†,‡,§] Stacy L. Capehart,[∥] Suchetan Pal,[⊥] Minghui Liu,[⊥] Lei Zhang,[†,‡] P. James Schuck,[†,‡] Yan Liu,[⊥] Hao Yan,[⊥] Matthew B. Francis,[†,∥] and James J. De Yoreo[†,‡,§,*]

[†]Materials Sciences Division, Lawrence Berkeley National Laboratory, Berkeley, California 94720, United States, [‡]The Molecular Foundry, Lawrence Berkeley National Laboratory, Berkeley, California 94720, United States, [§]Fundamental and Computational Sciences Directorate, Pacific Northwest National Laboratory, Richland, Washington 99352, United States, [∥]Department of Chemistry, University of California Berkeley, Berkeley, California 94720, United States, and [⊥]The Biodesign Institute and Department of Chemistry and Biochemistry, Arizona State University, Tempe, Arizona 85287, United States

ABSTRACT Building plasmonic nanostructures using biomolecules as scaffolds has shown great potential for attaining tunable light absorption and emission *via* precise spatial organization of optical species and antennae. Here we report bottom-up assembly of hierarchical plasmonic nanostructures using DNA origami templates and MS2 virus capsids. These serve as programmable scaffolds that provide molecular level control over the distribution of fluorophores and nanometer-scale control over their distance from a gold nanoparticle antenna. While previous research using DNA origami to assemble plasmonic nanostructures focused on determining the distance-dependent response of single fluorophores, here we address the challenge of constructing hybrid nanostructures that present an organized ensemble of fluorophores and then investigate the plasmonic response. By combining finite-difference time-domain numerical simulations with atomic force microscopy and correlated scanning confocal fluorescence microscopy, we find that the use of the scaffold keeps the majority of the fluorophores out of the quenching zone, leading to increased fluorescence intensity and mild levels of enhancement. The results show that the degree of enhancement can be controlled by exploiting capsid scaffolds of different sizes and tuning capsid–AuNP distances. These bioinspired plasmonic nanostructures provide a flexible design for manipulating photonic excitation and photoemission.

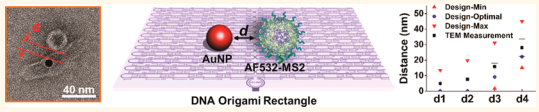

KEYWORDS: bioinspired assembly · DNA origami · virus capsid · plasmonic nanostructure · scanning confocal microscopy · atomic force microscopy (AFM) · finite-difference time-domain (FDTD) simulation

The use of biomolecules as scaffolds for directed organization of functional inorganic and organic nanomaterials addresses the grand challenge of assembling multiple functional units with precise control over their spatial arrangement at the molecular level. Peptides, proteins, and nucleic acids have been used as building blocks for the bottom-up assembly of intricate suprastructures due to their inherent chemical and biological addressability, structural precision, and efficiency of synthesis.[1−6] Inspired by natural photosynthesis systems, one appealing application of this bioinspired assembly strategy is to design artificial plasmonic structures through the integration of optical species, such as fluorophores or quantum dots, and conductive nanostructures that can manipulate light absorption and emission.[7−19] In a typical natural photosynthesis complex, the light-harvesting units are organized with molecular-level precision around the photochemical units so as to generate antenna complexes that ensure efficient photon absorption and energy transfer.[20] In a similar manner, biomimetic assembly of plasmonic nanostructures provides molecular-level spatial precision, creating potential improvement in efficiency of light-harvesting platforms, light-emitting devices, and optical sensors.[21−26]

DNA oligonucleotides have been used as tunable spacers to control the distance between gold nanoparticles (AuNPs) and fluorophores due to their sequence specificity and the spatial addressability.[5,27,28] In a major advance toward programmable structures, DNA origami has recently provided an alternative paradigm for biotemplating, acting as molecular pegboards to locate noble metal nanostructures, single dye molecules, and quantum dots.[8−12,29,30]

Additionally, virus capsids have recently been explored as versatile biological scaffolds

* Address correspondence to James.DeYoreo@pnnl.gov.

Received for review March 21, 2014 and accepted July 14, 2014.

Published online July 14, 2014
10.1021/nn5015819

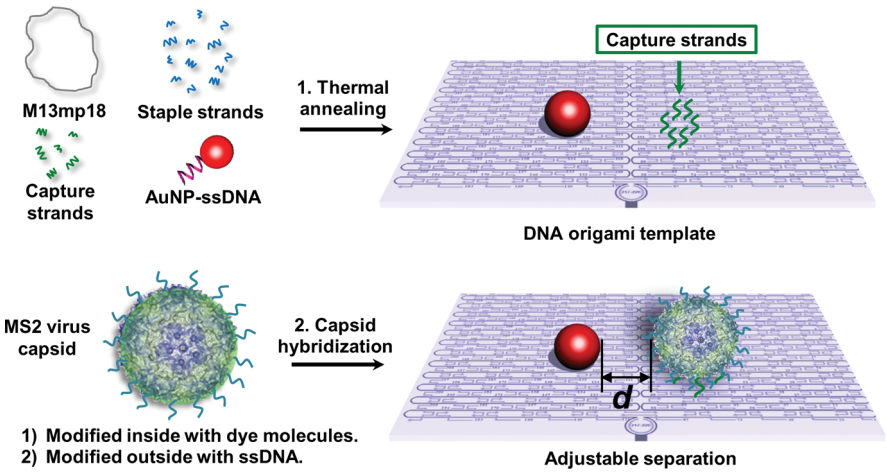

Figure 1. Assembly of hierarchical plasmonic nanostructures using DNA origami templates and MS2 virus capsids. A two-step thermal annealing process involves (1) incorporation of one ssDNA-modified AuNP and the capsid capture strands (6 strands extended with A_{20} per origami) into the DNA origami templates and (2) attachment of internally AF532 modified and externally DNA (T_{20}) modified MS2 virus capsids to the DNA origami templates. The distance between the two particles was adjusted by varying the position of the strand that linked to the AuNP surface.

for building functional nanostructures.[1,31] Virus capsids present tens to hundreds of equivalent sites that can be covalently modified to attach functional molecules (*e.g.*, a T3-type MS2 virus has 180 equivalent sites). Their exterior surfaces have been modified to display peptides,[32] polymers,[33] DNA,[34,35] and fluorophores,[36] whereas their interior surfaces have been modified to include fluorophores[34,35] and porphyrins.[37] Additionally, quantum dots and nanoparticles can be inserted inside the capsids.[36,3838]

Here we report hierarchical assembly of plasmonic structures using rectangular DNA origami templates and MS2 virus capsids as programmable molecular scaffolds to control both the distribution of fluorophores and their distance from a AuNP plasmonic antenna. While previous studies of DNA origami-based plasmonic nanostructures focused on the distance-dependent response of single-molecule fluorescence near noble metal nanoparticles,[11,27] in this work, we study the collective plasmon-coupled response of an ensemble of fluorophores to the presence of a AuNP at controlled distances. We show that the ensemble of fluorophores exhibits greater intensity than its single-molecule counterpart, because the size of the capsid scaffold keeps the majority of fluorophores out of the quenching region, and that the appropriate choice of capsid and particle dimensions, separation, and wavelength can lead to significant enhancement. This strategy is readily applicable to bottom-up assembly of complex nanophotonic architectures.

RESULTS AND DISCUSSION

We assembled the hierarchical plasmonic nanostructures by attaching a AuNP (Ted Pella, Inc., 10 nm diameter) and a fluorophore-modified MS2 capsid to a rectangular DNA origami template as illustrated in Figure 1. The rectangular template (length 90 nm, width 60 nm) was folded from one single-stranded M13mp18 ssDNA (~7200 nt long) using 226 single-stranded staple strands.[39] The AuNP was fixed onto the DNA origami by linking it to one staple strand whose 5′ end was modified with lipoic acid at the 5′ end. The 1:1 DNA-modified AuNP was then mixed with the scaffold M13 DNA and all the other staple strands, along with the capsid capture strands (poly A sequence extended from one end of the selected group of staple strands), in the first thermal annealing step. An N87C mutation was introduced to the MS2 capsid to allow for interior labeling with Alexa Fluor 532 maleimide dye (AF 532, Life Technologies). The dye labeling reaction had very high yield, reaching approximately 90 ± 5% of maximum loading capacity (*i.e.*, 150−170 AF532 molecules per capsid), giving a fluorophore density of one molecule per 14 nm^2 on the inside. An unnatural amino acid, *para*-amino-L-phenylalanine (*p*AF), was introduced at the capsid T19 position, which enabled us to further modify the capsids on the exterior surfaces with 20 nt poly-T sequences, at up to ~20 strands/capsid (~11% surface coverage), through a previously reported oxidative coupling reaction.[32] The internally dye modified and externally DNA modified capsids were then attached to the AuNP-decorated DNA origami through DNA hybridization in the second thermal annealing step.

We constructed four plasmonic structures (d1, d2, d3, and d4) by varying the location of the AuNP capture strands and hence the distance between the AuNP and the capsid as shown in Figure 2 (see Supporting Information for specific capture strand sequences). The attachment of the AuNP and the capsid to the DNA origami was confirmed by transmission electron microscopy (TEM), which also verified their actual separation distances. Because we incorporated six capture strands into the origami templates over an

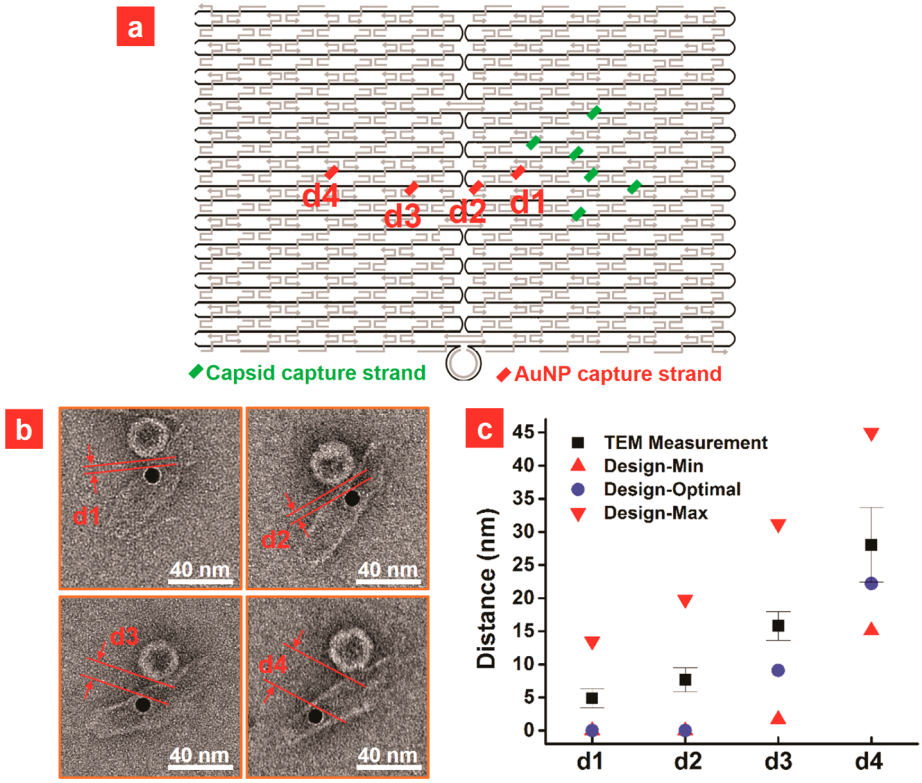

Figure 2. Control over the distance between an ensemble of AF532 fluorophores and a AuNP in the DNA origami–capsid nanostructures. (a) Schematic of DNA origami template design showing the locations of the capture strands for the capsid and the strand linked to the AuNP. The control over the distance between the dye-modified capsid and the AuNP is enabled by varying the location of the AuNP linkage strand (d1, d2, d3, and d4). (b) TEM images of the hierarchical nanostructures with four different distances. (c) Statistics from TEM imaging analysis of d1–d4 (total n = 83) shown in comparison with the designed ranges as indicated by design-min, design-max, and design-optimal.

area within a 10 nm radius in order to maximize the immobilization efficiency, we calculated the range of edge-to-edge capsid–AuNP distances from the DNA origami design scheme. The minimum, maximum, and optimal distances were calculated assuming the capsid is attached to the nearest, farthest, and center of the capture strands as shown in Figure 2c. The TEM measurements yielded rather narrow distributions of the capsid–AuNP distances, with d1 = 4.9 ± 1.5 nm, d2 = 7.7 ± 1.8 nm, d3 = 15.8 ± 2.2 nm, and d4 = 28.0 ± 5.6 nm, which are near the centers of the design ranges. Note that although we tried to minimize the capsid–AuNP spacing, the lower limit we were able to achieve was 4.9 nm for d1, presumably because a strong coupling interaction prevented the pair from reaching closer proximity.[40]

High-resolution tapping mode atomic force microscopy (AFM) imaging was also used to characterize the assembled structures. AFM images provided three-dimensional profiles of the DNA origami templates, capsids, and AuNPs, hence a routine method to distinguish the AuNPs from the capsids (Figure 3a). The measured AuNP height distribution of 9.7 ± 0.7 nm matched well with the nominal AuNP diameter of 10 nm (Figure 3b). The capsids, however, did not maintain their spherical shape when deposited on mica substrates and scanned under an AFM tip. Their measured heights of 8.0 ± 1.0 nm were about one-third of their 27 nm diameters,[35] as obtained by scanning transmission electron microscopy (STEM) (Figure 3c). The capsid widths of around 35 nm determined by AFM were significantly larger than those measured by STEM (Figure 3c). Although AFM provides precise height measurements up to ~0.08 nm resolution, tip convolution artifacts lead to significant overestimates of lateral dimensions.[41] In addition, STEM imaging confirmed the icosahedral symmetry of the MS2 capsids, with the majority exhibiting hexagonal cross sections. From the STEM-based statistics of the long (a) and short (b) diagonals, we obtained an asymmetry factor (a/b) of 1.10 ± 0.14, which is consistent with the asymmetry of an equilateral hexagon for which a/b = 1.16. Nevertheless, the high precision of the AFM height measurements enabled us to obtain a detailed perspective of the top surface morphology of the capsids not obtainable by transmission imaging methods such as TEM or STEM. Figure 3d demonstrates a fairly smooth top surface of the capsids, showing a root-mean-square (RMS) roughness value of 0.7 ± 0.1 nm, in comparison with its thickness of 8.0 nm as measured by the AFM height profiling. Therefore, we modeled the capsid deposited onto a flat mica surface

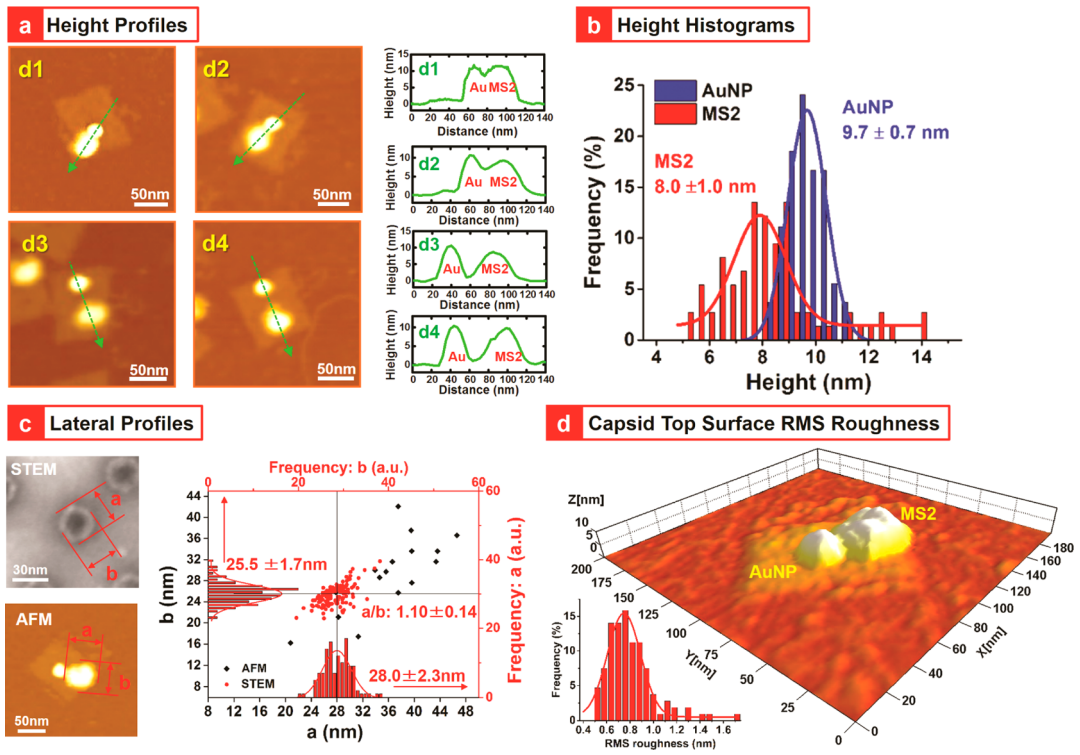

Figure 3. AFM three-dimensional topography analysis. (a) AFM topography images and height profiles of assembled hierarchical nanostructures with different interparticle distances, d1, d2, d3, and d4. (b) Histograms showing the height distribution of the AuNPs and the capsids on DNA origami templates as measured by AFM (n = 54 for AuNP, n = 74 for MS2 capsids). (c) Histograms showing the lateral profiles of the capsids as measured by STEM and AFM (n = 122 for STEM analysis, n = 16 for AFM analysis). (d) RMS roughness histogram revealing the morphology of capsids' top surface when deposited on mica substrates (n = 107).

as a cylinder of low aspect ratio, with a height of 8 nm and diameter of 27 nm.

By correlating the AFM images with the scanning confocal fluorescence microscopy images, we were able to simultaneously validate the identities of fluorescent particles—determining whether they were either excess unbound capsids or capsids bound to the origami templates—and measure the fluorescence intensity as a function of the edge-to-edge distance between the capsids and the AuNPs. To perform these measurements, one 2 μL aliquot of sample solution (in 2× TAE-Mg^{2+} buffer) was deposited on a poly-L-lysine (Ted Pella, Inc.)-coated mica substrate (SPI Supplies). The samples were diluted to ensure adjacent plasmonic nanostructures were a couple of micrometers away from one another when deposited onto the mica surface. This was necessary to optically resolve fluorescent particles considering the diffraction limit of the optics, which can be estimated by $\lambda/(2\cdot NA) \approx 280$ nm, for a 532 nm laser illumination using a NA = 0.95 100× air objective. The sample was washed with milli-Q water (18 MΩ·cm^{-1}) and dried with a gentle stream of nitrogen gas before measurements.

Immediately after the sample was prepared, scanning confocal fluorescence images were acquired by raster scanning the sample in the focal plane of the incident 532 nm laser beam and by mapping the fluorescence emission using a WITEC scanning confocal optical microscope. In this setup, a single counting photomultiplier tube (PMT) detector was used to record the fluorescence emission through a long-pass emission filter with cut-on wavelength of 550 nm, which corresponds to the AF532 peak emission wavelength. The samples were then transferred to an AFM (Veeco Multimode VIII) for tapping mode topographical imaging at moderate resolution (380 nm^2/pixel). We were able to retrieve the locations of the same particles seen in the confocal fluorescence imaging with the aid of visual marks patterned on the mica substrate. Figure 4a shows a typical correlative imaging analysis as described above (see Figure S3 in the Supporting Information for more information). Higher resolution tapping mode AFM topographical images (4 nm^2/pixel, Figure 4b and c) were then used to distinguish the capsid−AuNP pairs from the unbound capsids in the fluorescence images (as highlighted in the red and yellow dashed-line box in Figure 4a, respectively). The small particle in the center of the DNA origami template was determined to be the AuNP from its ∼10 nm height profile (Figure 4b, #1). The mismatch between the measured width (25 nm) and its nominal diameter (10 nm) is due to tip convolution described above.[41] The particle near the AuNP was determined to be a capsid from its height of 8 nm and

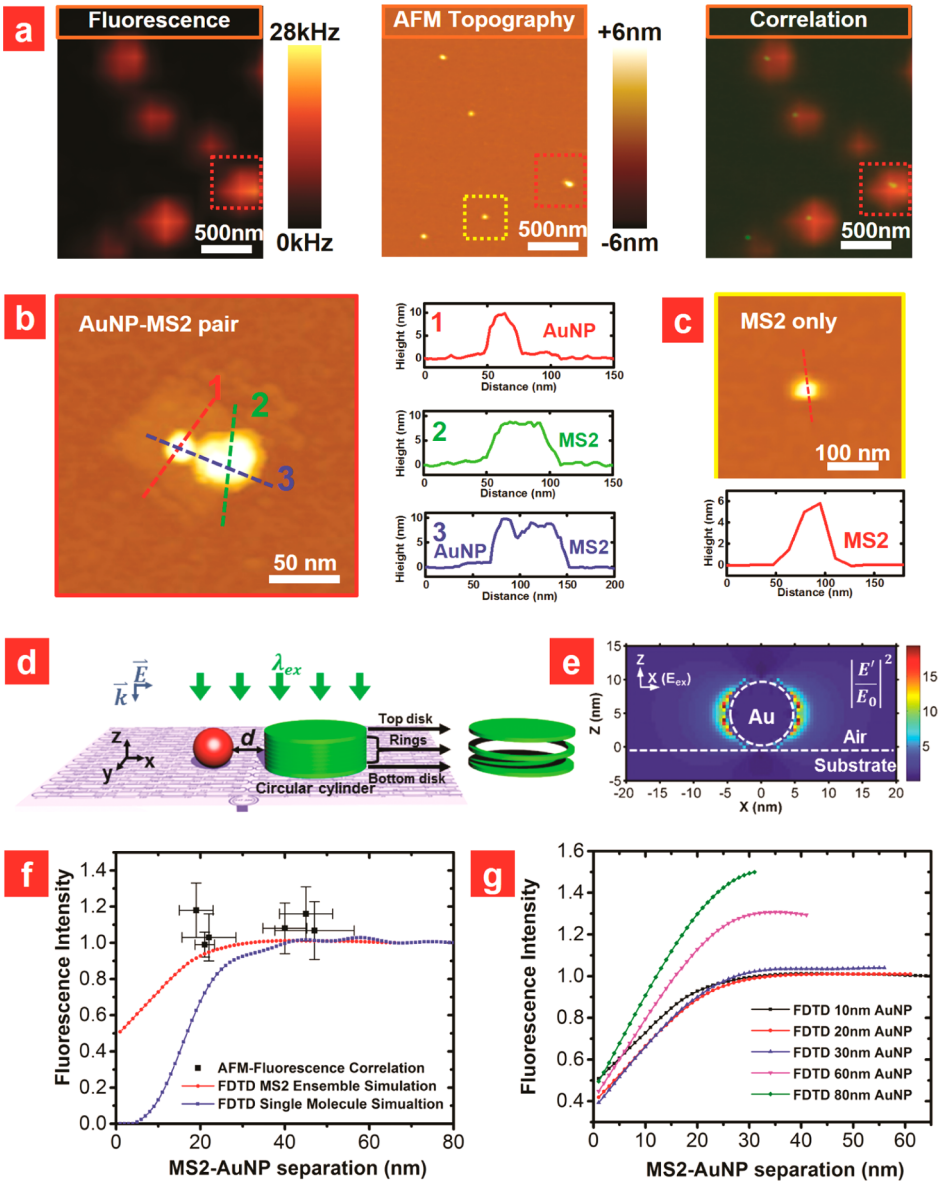

Figure 4. AFM correlated scanning confocal fluorescence microscopy and FDTD numerical simulations of the plasmon-coupled response of the hierarchical nanostructures. (a) Work flow of the AFM-confocal fluorescence correlation. After scanning confocal fluorescence microscopy images were acquired, high-resolution AFM imaging was used to correlate with the fluorescence images. The identities of the two fluorescent particles boxed in the red and yellow dashed line boxes were confirmed to be an assembled AuNP−capsid on the same DNA origami and an unbound capsid, respectively. Higher resolution AFM images with the cross-section height profiles are shown in (b) and (c), respectively. (d) Modeling of the plasmonic behavior of the DNA origami−capsid nanostructure. The capsid can be viewed as a hollow circular cylinder in which the dye molecules are uniformly distributed on the top, bottom, and side surfaces. (e) Electric field intensity distribution map for a 10 nm AuNP at λ = 532 nm obtained from FDTD simulation based on the Mie scattering model. (f) Plot of experimental data from AFM-fluorescence correlation in comparison with FDTD simulation results for single-molecule fluorescence and ensemble fluorescence. The horizontal and vertical error bars of the experimental results represent the tip convolution in AFM imaging and variation in capsid fluorescence intensity, respectively. Note that six groups of experimental data from experiments were plotted to represent the d1−d4 design. (g) FDTD prediction of the AuNP size dependence of the ensemble fluorescence.

widths of 47 and 57 nm (Figure 4b, #2 and #3). The center-to-center distance of capsid−AuNP is measured to be 38 nm. Thus, the edge-to-edge separation between the two was determined to be ~19.5 nm by subtracting the radius of the AuNP (5 nm) and the radius of the MS2 capsid (13.5 nm). Here the deviation in the AFM width measurements of capsids and AuNPs from those obtained by electron microscopy (Figure 3c) is again due to the intrinsic tip convolution and tip-induced capsid deformation in AFM imaging.

To gain a predictive physical understanding of the light absorption and emission behaviors of these hierarchical plasmonic nanostructures, we carried out finite-difference time-domain (FDTD) numerical simulations to calculate the distance dependence of emission rate for the dye molecules on the capsid with

respect to the AuNP (see Figure S4 in the Supporting Information for details). Because the capsids have a cylindrical shape as determined by the TEM, STEM, and AFM measurements (Figures 2 and 3), we assumed the dye molecules were distributed over the surface of a hollow circular cylinder rather than on a sphere (Figure 4d). We further assumed a uniform distribution on the top, bottom, and side surfaces of the circular cylinder, because of the high dye loading level on the inner surface of the capsid. For simplicity of calculation, the top and bottom surfaces were viewed as circular disks of 1 nm thickness, and the side surface of the cylinder was further divided into six concentric rings with 1 nm thickness that stacked between the top and the bottom disks. Based on the dye loading of $90 \pm 5\%$ of the 180 available attachment sites, the top and bottom disk then each contained ~51 dye molecules and each concentric ring contained ~10 dye molecules, giving approximately uniform number density over the capsid surface.

The fluorescence emission rate γ_{em} is determined by a two-step process and can be expressed as the product of the excitation rate γ_{ex} that captures the effect of the local excitation field and the quantum yield q that represents the emission probability.[21] Figure 4e depicts the electric field intensity distribution map for a 10 nm AuNP at $\lambda = 532$ nm from the FDTD simulation based on the Mie scattering model.[42] This vertical cross section map shows that the electric field enhancement occurs near the AuNP, which leads to improved excitation rates and enhanced absorption of the light. In addition, the field enhancement drops rapidly beyond $d = \sim 5$ nm on the equatorial plane ($Z = 5$ nm) and even more rapidly on the substrate surface plane ($Z = 0$ nm) and the particle's top plane ($Z = 10$ nm), indicating a Z-dependent field enhancement profile. The quantum yield q of a single-molecule fluorescence was calculated from an FDTD simulation where the dye molecule was modeled as a dipole near a AuNP. The radiative and nonradiative decay rates from the simulation were used to calculate the emission rate γ_{em} of a single AF532 molecule as shown in Figure 4f (see the Supporting Information for FDTD simulation details). The simulation result suggests a significant quenching of the emission rate for a single dye molecule when $d < 20$ nm, because the decrease of quantum yield wins over the increase of excitation rate. This quenching phenomenon is consistent with many previous studies from both theoretical calculations and experimental observations on single-molecule fluorescence behavior.[11,21,27] However, since the capsid acts as a molecular scaffold for the three-dimensional organization of AF 532 molecules, it opens new possibilities beyond planar organization of dye molecules and allows us to evaluate the plasmonic response of the entire ensemble of the dye molecules on the capsid. In Figure 4f, we show the FDTD simulation results of a single-molecule fluorescence case (blue dashed line) and for the case of an ensemble of fluorophores on a cylinder as discussed above (red dashed line), respectively. The ensemble fluorescence can raise the emission rate in the single-molecule quenching regime where $d < 20$ nm, because the size of the virus capsid is much larger than the AuNP, so that the majority of the dye molecules stay out of the quenching zone and less than 39% are located in the region where fluorescence is significantly affected by the AuNP. This can explain the weak distance dependence of the measured fluorescence intensity outside and near the single-molecule quenching regime ($d < 20$ nm). Figure 4f shows a good agreement between the AFM-fluorescence correlation measurements and the FDTD simulations of ensemble fluorescence.

The capsid size effect on fluorescence emission rate is further illustrated in Figure 4g, where we show the FDTD predictions for the effect of increasing the AuNP size, from 10 nm to 20 nm, 30 nm, 60 nm, and 80 nm. For 60 and 80 nm AuNPs, for which the size is much larger than that of the capsid, the quenching regime is reduced to $d < \sim 12$ nm and an emission enhancement is predicted. Because there exists a diverse collection of virus capsids with diameters ranging from 9 to 31 nm,[1,31] the results in Figure 4g imply that one can select a capsid species as a template for which the size is comparable to the AuNPs in order to achieve the desired control over the fluorescence intensity.

CONCLUSIONS

In summary, we have demonstrated the use of DNA origami templates and MS2 virus capsids as spatially addressable scaffolds for constructing hierarchical plasmonic nanostructures in which AuNPs serve as plasmonic antennae. We have shown tight control over the distance between capsid−nanoparticle surfaces, which is possible due to the programmable nature of the DNA origami template and the ability to site-specifically modify the MS2 virus capsid scaffold. The judicial choice of dye molecules organized in 3D on the virus scaffold can effectively increase the fluorescence intensity because of the size of the capsid. Moreover, FDTD simulations show that increasing the size of the AuNPs to be commensurate with that of the capsids and the choice of illumination wavelength to optimize the plasmonic antenna effect can enable significant fluorescence enhancement.

We believe that the intensive research activities in DNA origami and virus capsid scaffolds hold promise for bringing added optical species and chemical moieties to this biomimetic assembly strategy for building more robust plasmonic nanostructures. Our future studies will focus on improving the design of plasmonic structures by exploring an extended variety of metal species, nanoparticle shapes, and spectral

properties of fluorophores to achieve optimal interaction and enhancement of photoemission.[43] This bioinspired approach to building plasmonic nanostructures may address the need for multicomponent plasmonic systems for future optical and optoelectronic applications.

MATERIALS AND METHODS

Activation of Lipoic Acid to Synthesize NHS Ester of Lipoic Acid. *N,N′*-Dicyclohexylcarbodiimide (DCC, 2.10 g, 10 mmol) was mixed with lipoic acid (2.06 g, 10 mmol) in tetrahydrofuran (THF, 10 mL) followed by the addition of *N*-hydroxysuccinimide (NHS, 1.15 g, 10 mmol). The reaction mixture was filtered (using filter paper) after stirring continuously for 72 h. The filtrate was evaporated to obtain a crystalline solid. The NHS ester of lipoic acid was further purified by recrystallization from toluene.

Conjugation of Lipoic Acid with Amine-Modified Oligonucleotides. The NHS ester of lipoic acid prepared as described above was added in excess to 5′-amine-modified oligonucleotide in a solution of 70% acetonitrile and 30% water (pH ∼8). The reaction mixture was kept overnight at room temperature. The lipoic acid-conjugated oligonucleotide was purified by microspin G25 columns (GE Healthcare) and used for the next step.

Phosphination and Concentration of AuNPs. AuNPs (10 nm, Ted Pella Inc.) were stabilized with adsorption of bis-*p*-sulfonatophenylphosphene dihydrate, dipotassium salt (BSPP, Strem Chemicals). Phosphine coating increases the negative charge on the particle surface and, therefore, stabilizes the AuNPs in high electrolyte concentrations at a higher particle density. BSPP (15 mg) was added to the colloidal nanoparticle solution (50 mL, particle density 5.7 × 1012/mL), and the mixture was shaken overnight at room temperature. Sodium chloride (solid) was added slowly to this mixture while stirring until the color changed from deep burgundy to light purple. The resulting mixture was centrifuged at 3000 rpm for 30 min, and the supernatant was carefully removed with a pipet. AuNPs were then resuspensed in a 1 mL solution of BSPP (2.5 mM). Upon mixing with 1 mL of methanol, the mixture was centrifuged, the supernatant was removed, and the AuNPs were resuspended in 1 mL of BSPP solution (2.5 mM). The concentration of the AuNPs was estimated from the optical absorbance at ∼520 nm.

Preparation of AuNP−DNA Conjugates with Discrete Numbers of DNA Strands. The lipoic acid-modified DNAs were incubated with an equimolar ratio of phosphinated AuNPs in 1× TBE buffer (89 mM Tris, 89 mM boric acid, 2 mM EDTA, pH 8.0) containing 50 mM NaCl overnight at room temperature. AuNP−DNA conjugates with discrete numbers of oligonucleotides were separated by 3% agarose gel (running buffer 0.5× TBE, loading buffer 50% glycerol, 15 V/cm, 25 μL load volume).[2] The band with a 1:1 ratio of AuNP/DNA was electroeluted into the glass fiber filter membrane, backed by dialysis membrane (MWCO 10000). AuNP−DNA conjugates were recovered using a 0.45 μm pore size centrifugal filter device. The concentration of these AuNP−DNA conjugates was estimated from the optical absorbance at ∼520 nm.

Self-Assembly of DNA Origami with One AuNP. The molar ratio of the M13 ssDNA, the 1:1 DNA−AuNP conjugate, the staple strands (unpurified), and the capture strands was 1:1:5:5. The mixture solution was annealed in 1× TBE buffer with 0.5 M NaCl by cooling slowly from 65 °C to 4 °C. In order to remove the excess staple strands and to exchange the buffer, the resultant solution was purified by a Microcon filtration device (100 kDa MWCO) and washed with 0.5× TAE-Mg.

Preparation of DNA Origami Templates. To assemble the rectangular-shaped DNA origami, 5 nM single-stranded M13mp18 DNA (NEB, 7249 nt long) is mixed with the staple strands (unpurified) and six capture strands (IDTDNA denaturing PAGE purified, detailed sequences later) in 1:5:5 molar ratio, following the design outlined in the literature in 0.5× TAE-Mg^{2+} (20 mM Tris, 10 mM acetic acid, 1 mM EDTA, and 6.2 mM magnesium acetate, pH 8.0).[1] The resulting solution was cooled from 95 °C to 4 °C to form the DNA origami structures. It was then purified using a Microcon centrifugal filtration device (100 kDa MWCO filters, Millipore, Bedford, MA, USA) to remove the excess staple strands.

Assembly of AuNPs and MS2 Capsids on DNA Origami Templates. The mixture of M13 ssDNA, the ssDNA−AuNP conjugate, the staple strands (unpurified), and the capture strands (molar ratio: 1:1:5:5) was annealed in 1× TBE buffer with 0.5 M NaCl by cooling slowly from 65 °C to 4 °C. In order to get rid of excess staple strands and to exchange the buffer, the resultant solution was purified by a Microcon filtration device (100 kDa MWCO) and washed with 0.5× TAE-Mg^{2+} buffer. Once the AuNP-modified origami structures (∼5 nM concentration) were prepared, they were mixed with MS2 virus capsids modified inside with maleimide-terminated AF532 dye molecules (Invitrogen, Life Technologies) and outside with 20 nt poly-T sequence ssDNA in 1:5 molar ratio and annealed. For annealing reactions between capsids and templates, the components were mixed in 0.5× TAE-Mg^{2+} buffer and annealed from 37 °C to 4 °C at a rate of 1 °C/min on a S1000 Thermal Cycler PCR machine (Bio-Rad, USA). Typical final origami concentrations were ∼2 nM, and the capsid concentration was 4 times that of the origami concentration.

TEM, STEM, and AFM-Correlated Confocal Fluorescence Microscopy. Near-field confocal fluorescence imaging was carried out on a WITec Alpha 300 S scanning near-field optical microscope. A frequency-doubled Nd:YAG solid-state laser was used to supply a single-mode 532 nm laser for AF532 dye excitation. The laser was focused by a Nikon 100× near-field air objective (Nikon CFI LU Plan Apo EPI 100×, NA = 0.95, WD = 0.4 mm). The laser power was maintained at ∼1 μW to avoid excessive photobleaching of the dye molecules. A typical scanning confocal fluorescence image was taken in a 15 μm × 15 μm area with 100 × 100 pixel spatial resolution and 100 ms dwell time at each pixel. The fluorescence intensity signal was recorded by a single photon counting PMT detector (Hamamatsu Photonics, typical QE 15%, and dark count rate <100 cps). Tapping mode AFM topographical imaging was performed on a Veeco Multimode VIII AFM system. Ultrasharp AFM tips (Nanoworld AG, tip radius <10 nm, k = 2.8 N/m, f = 75 kHz) were used to acquire high spatial resolution operating in tapping mode. The 2D and 3D AFM images were processed and analyzed with SPIP software (Image Metrology A/S). The STEM image of d1 and TEM images of d2, d3, and d4 as shown in Figure 1b were collected by a Zeiss Ultra55 Analytical FESEM equipped with STEM detector and a Zeiss Libra 120 Plus TEM, respectively. Prior to the transmission electron microscopy imaging, a 2 μL aliquot of sample solution was applied to ultrathin carbon film coated Cu grids (Ted Pella, Inc.) that had been cleaned with oxygen plasma (Harrick Plasma). An optimized negative-staining step was applied to the sample for improved contrast during TEM imaging.[44,45]

FDTD Numerical Simulations. We performed FDTD simulations using a commercial software package: FDTD Solutions from Lumerical Solutions, Inc. In the Mie 3D simulation, a total-field scattered-field plane wave source propagating along the *Z*-axis was used. In the quantum yield simulation, the dye molecule was modeled as a dipole near a AuNP. A uniform mesh size in *x*, *y*, and *z* directions of 0.5 nm was used for Mie 3D simulation, and 1.0 nm was used for the quantum yield simulation. In both calculations, the AuNP was modeled as a sphere, its optical constants of gold were taken from Johnson and Christy[46] in the spectrum range from 300 to 800 nm, and perfectly matched layer boundary conditions were set for *x*, *y*, and *z* directions. Since the fluorescence emission rate γ_{em} is a two-step process that can be expressed as the product of excitation rate γ_{ex} and the quantum yield *q*, we first calculated the single-dye fluorescence emission rate from the Mie 3D and quantum yield simulations (see Figure S4 in the Supporting Information). The Mie 3D simulation generated an electric field enhancement

profile near the AuNP surface that reflects the enhancement of the excitation rate γ_{ex}.[21] The radiative and nonradiative decay rates calculated from the quantum yield simulation were used to calculate the quantum yield of the dye molecule. The dye molecule ensemble is the entire collection of the dye molecules labeled on the interior surface of the capsid; we assumed their ensemble fluorescence to be the superposition of the individual dye molecules to the first order. From the single-molecule calculation results (Figure 4e and f), we learned that the emission rate of a dye molecule depends on its distance to the AuNP and its *z*-height with respect to the substrate. On the basis of the modeling scheme as illustrated in Figure 4d, the ensemble fluorescence was calculated from the weighted average emission rates of individual dye molecules uniformly distributed on the top and bottom surfaces (viewed as disks) and the side surface (further divided into concentric rings) of a circular cylinder.

Conflict of Interest: The authors declare no competing financial interest.

Acknowledgment. This work was performed at Lawrence Berkeley National Laboratory and Pacific Northwest National Laboratory with support from the U.S. Department of Energy Office of Science, Office of Basic Energy Sciences, Division of Materials Science and Engineering, under Contract Nos. DE-AC02-05CH11231 and DE-AC05-76RL01830, respectively. Research was carried out in the Molecular Foundry, Lawrence Berkeley National Laboratory, which is supported by the U.S. Department of Energy Office of Science, Office of Basic Energy Sciences, Scientific User Facilities Division. S.L.C. was supported by an NSF graduate research fellowship (2010101391). Work performed at Arizona State University was supported by grants from the Office of Naval Research. We thank Dr. Gang Ren for his supervision of the TEM imaging work. We thank Dr. Jeffery Neaton, Dr. Sahar Sharifzadeh, and Andrew Taber for their constructive discussions on the FDTD simulation. We thank Dr. Jolene Lau for assistance with the protein and capsid biochemistry. Pacific Northwest National Laboratory is a multiprogram national laboratory operated for the U.S. Department of Energy by Battelle.

Supporting Information Available: DNA origami capture strand details, Figures S1−S4, and Tables S1−S2 are available free of charge *via* the Internet at http://pubs.acs.org.

REFERENCES AND NOTES

1. Douglas, T.; Young, M. Viruses: Making Friends with Old Foes. *Science* **2006**, *312*, 873–875.
2. Pinheiro, A. V.; Han, D.; Shih, W. M.; Yan, H. Challenges and Opportunities for Structural DNA Nanotechnology. *Nat. Nanotechnol.* **2011**, *6*, 763–772.
3. Tan, S. J.; Campolongo, M. J.; Luo, D.; Cheng, W. L. Building Plasmonic Nanostructures with DNA. *Nat. Nanotechnol.* **2011**, *6*, 268–276.
4. Fischlechner, M.; Donath, E. Viruses as Building Blocks for Materials and Devices. *Angew. Chem., Int. Ed.* **2007**, *46*, 3184–3193.
5. Storhoff, J. J.; Mirkin, C. A. Programmed Materials Synthesis with DNA. *Chem. Rev.* **1999**, *99*, 1849–1862.
6. Zhang, S. G. Fabrication of Novel Biomaterials through Molecular Self-Assembly. *Nat. Biotechnol.* **2003**, *21*, 1171–1178.
7. Stein, I. H.; Steinhauer, C.; Tinnefeld, P. Single-Molecule Four-Color FRET Visualizes Energy-Transfer Paths on DNA Origami. *J. Am. Chem. Soc.* **2011**, *133*, 4193–4195.
8. Deng, Z.; Samanta, A.; Nangreave, J.; Yan, H.; Liu, Y. Robust DNA-Functionalized Core/Shell Quantum Dots with Fluorescent Emission Spanning from UV-Vis to Near-IR and Compatible with DNA-Directed Self-Assembly. *J. Am. Chem. Soc.* **2012**, *134*, 17424–17427.
9. Pal, S.; Deng, Z. T.; Ding, B. Q.; Yan, H.; Liu, Y. DNA-Origami-Directed Self-Assembly of Discrete Silver-Nanoparticle Architectures. *Angew. Chem., Int. Ed.* **2010**, *49*, 2700–2704.
10. Acuna, G. P.; Moller, F. M.; Holzmeister, P.; Beater, S.; Lalkens, B.; Tinnefeld, P. Fluorescence Enhancement at Docking Sites of DNA-Directed Self-Assembled Nanoantennas. *Science* **2012**, *338*, 506–510.
11. Acuna, G. P.; Bucher, M.; Stein, I. H.; Steinhauer, C.; Kuzyk, A.; Holzmeister, P.; Schreiber, R.; Moroz, A.; Stefani, F. D.; Liedl, T.; *et al*. Distance Dependence of Single-Fluorophore Quenching by Gold Nanoparticles Studied on DNA Origami. *ACS Nano* **2012**, *6*, 3189–3195.
12. Schmied, J. J.; Forthmann, C.; Pibiri, E.; Lalkens, B.; Nickels, P.; Liedl, T.; Tinnefeld, P. DNA Origami Nanopillars as Standards for Three-Dimensional Superresolution Microscopy. *Nano Lett.* **2013**, *13*, 781–785.
13. Stein, I. H.; Schuller, V.; Bohm, P.; Tinnefeld, P.; Liedl, T. Single-Molecule FRET Ruler Based on Rigid DNA Origami Blocks. *ChemPhysChem* **2011**, *12*, 689–695.
14. Kuzyk, A.; Schreiber, R.; Fan, Z. Y.; Pardatscher, G.; Roller, E. M.; Hogele, A.; Simmel, F. C.; Govorov, A. O.; Liedl, T. DNA-Based Self-Assembly of Chiral Plasmonic Nanostructures with Tailored Optical Response. *Nature* **2012**, *483*, 311–314.
15. Dutta, P. K.; Varghese, R.; Nangreave, J.; Lin, S.; Yan, H.; Liu, Y. DNA-Directed Artificial Light-Harvesting Antenna. *J. Am. Chem. Soc.* **2011**, *133*, 11985–11993.
16. Pal, S.; Dutta, P.; Wang, H.; Deng, Z. T.; Zou, S. L.; Yan, H.; Liu, Y. Quantum Efficiency Modification of Organic Fluorophores Using Gold Nanoparticles on DNA Origami Scaffolds. *J. Phys. Chem. C* **2013**, *117*, 12735–12744.
17. Ming, T.; Chen, H. J.; Jiang, R. B.; Li, Q.; Wang, J. F. Plasmon-Controlled Fluorescence: Beyond the Intensity Enhancement. *J. Phys. Chem. Lett.* **2012**, *3*, 191–202.
18. Zhang, J.; Fu, Y.; Chowdhury, M. H.; Lakowicz, J. R. Metal-Enhanced Single-Molecule Fluorescence on Silver Particle Monomer and Dimer: Coupling Effect between Metal Particles. *Nano Lett.* **2007**, *7*, 2101–2107.
19. Fu, Y.; Zhang, J.; Lakowicz, J. R. Plasmonic Enhancement of Single-Molecule Fluorescence near a Silver Nanoparticle. *J. Fluoresc.* **2007**, *17*, 811–816.
20. Bahatyrova, S.; Frese, R. N.; Siebert, C. A.; Olsen, J. D.; van der Werf, K. O.; van Grondelle, R.; Niederman, R. A.; Bullough, P. A.; Otto, C.; Hunter, C. N. The Native Architecture of a Photosynthetic Membrane. *Nature* **2004**, *430*, 1058–1062.
21. Anger, P.; Bharadwaj, P.; Novotny, L. Enhancement and Quenching of Single-Molecule Fluorescence. *Phys. Rev. Lett.* **2006**, *96*, 113002.
22. Lee, K. S.; El-Sayed, M. A. Gold and Silver Nanoparticles in Sensing and Imaging: Sensitivity of Plasmon Response to Size, Shape, and Metal Composition. *J. Phys. Chem. B* **2006**, *110*, 19220–19225.
23. Link, S.; El-Sayed, M. A. Size and Temperature Dependence of the Plasmon Absorption of Colloidal Gold Nanoparticles. *J. Phys. Chem. B* **1999**, *103*, 4212–4217.
24. Malicka, J.; Gryczynski, I.; Gryczynski, Z.; Lakowicz, J. R. Effects of Fluorophore-to-Silver Distance on the Emission of Cyanine-Dye-Labeled Oligonucleotides. *Anal. Biochem.* **2003**, *315*, 57–66.
25. Cang, H.; Labno, A.; Lu, C. G.; Yin, X. B.; Liu, M.; Gladden, C.; Liu, Y. M.; Zhang, X. Probing the Electromagnetic Field of a 15-Nanometre Hotspot by Single Molecule Imaging. *Nature* **2011**, *469*, 385–389.
26. Willets, K. A. Probing Local Electromagnetic Field Enhancements on the Surface of Plasmonic Nanoparticles. *Prog. Surf. Sci.* **2012**, *87*, 209–220.
27. Chhabra, R.; Sharma, J.; Wang, H. N.; Zou, S. L.; Lin, S.; Yan, H.; Lindsay, S.; Liu, Y. Distance-Dependent Interactions between Gold Nanoparticles and Fluorescent Molecules with DNA as Tunable Spacers. *Nanotechnology* **2009**, *20*, 485201.
28. Cheng, W. L.; Campolongo, M. J.; Cha, J. J.; Tan, S. J.; Umbach, C. C.; Muller, D. A.; Luo, D. Free-Standing Nanoparticle Superlattice Sheets Controlled by DNA. *Nat. Mater.* **2009**, *8*, 519–525.
29. Wang, Z. G.; Song, C.; Ding, B. Functional DNA Nanostructures for Photonic and Biomedical Applications. *Small* **2013**, *9*, 2210–2212.
30. Rothemund, P. W. K. Folding DNA to Create Nanoscale Shapes and Patterns. *Nature* **2006**, *440*, 297–302.
31. Uchida, M.; Klem, M. T.; Allen, M.; Suci, P.; Flenniken, M.; Gillitzer, E.; Varpness, Z.; Liepold, L. O.; Young, M.; Douglas,

T. Biological Containers: Protein Cages as Multifunctional Nanoplatforms. *Adv. Mater.* **2007**, *19*, 1025–1042.
32. Carrico, Z. M.; Romanini, D. W.; Mehl, R. A.; Francis, M. B. Oxidative Coupling of Peptides to a Virus Capsid Containing Unnatural Amino Acids. *Chem. Commun.* **2008**, *44*, 1205–1207.
33. Kovacs, E. W.; Hooker, J. M.; Romanini, D. W.; Holder, P. G.; Berry, K. E.; Francis, M. B. Dual-Surface-Modified Bacteriophage MS2 as an Ideal Scaffold for a Viral Capsid-Based Drug Delivery System. *Bioconjugate Chem.* **2007**, *18*, 1140–1147.
34. Tong, G. J.; Hsiao, S. C.; Carrico, Z. M.; Francis, M. B. Viral Capsid DNA Aptamer Conjugates as Multivalent Cell-Targeting Vehicles. *J. Am. Chem. Soc.* **2009**, *131*, 11174–11178.
35. Stephanopoulos, N.; Liu, M. H.; Tong, G. J.; Li, Z.; Liu, Y.; Yan, H.; Francis, M. B. Immobilization and One-Dimensional Arrangement of Virus Capsids with Nanoscale Precision Using DNA Origami. *Nano Lett.* **2010**, *10*, 2714–2720.
36. Capehart, S. L.; Coyle, M. P.; Glasgow, J. E.; Francis, M. B. Controlled Integration of Gold Nanoparticles and Organic Fluorophores Using Synthetically Modified MS2 Viral Capsids. *J. Am. Chem. Soc.* **2013**, *135*, 3011–3016.
37. Stephanopoulos, N.; Tong, G. J.; Hsiao, S. C.; Francis, M. B. Dual-Surface Modified Virus Capsids for Targeted Delivery of Photodynamic Agents to Cancer Cells. *ACS Nano* **2010**, *4*, 6014–6020.
38. Ashley, C. E.; Carnes, E. C.; Phillips, G. K.; Durfee, P. N.; Buley, M. D.; Lino, C. A.; Padilla, D. P.; Phillips, B.; Carter, M. B.; Willman, C. L.; *et al*. Cell-Specific Delivery of Diverse Cargos by Bacteriophage MS2 Virus-Like Particles. *ACS Nano* **2011**, *5*, 5729–5745.
39. Sharma, J.; Chhabra, R.; Andersen, C. S.; Gothelf, K. V.; Yan, H.; Liu, Y. Toward Reliable Gold Nanoparticle Patterning on Self-Assembled DNA Nanoscaffold. *J. Am. Chem. Soc.* **2008**, *130*, 7820–7821.
40. Sperling, R. A.; Parak, W. J. Surface Modification, Functionalization and Bioconjugation of Colloidal Inorganic Nanoparticles. *Philos. Trans. R. Soc. A* **2010**, *368*, 1333–1383.
41. Chen, S.-w. W.; Odorico, M.; Meillan, M.; Vellutini, L.; Teulon, J.-M.; Parot, P.; Bennetau, B.; Pellequer, J.-L. Nanoscale Structural Features Determined by AFM for Single Virus Particles. *Nanoscale* **2013**, *5*, 10877–10886.
42. Mie, G. Articles on the Optical Characteristics of Turbid Tubes, Especially Colloidal Metal Solutions. *Ann. Phys.-Berlin* **1908**, *25*, 377–445.
43. Darvill, D.; Centeno, A.; Xie, F. Plasmonic Fluorescence Enhancement by Metal Nanostructures: Shaping the Future of Bionanotechnology. *Phys. Chem. Chem. Phys.* **2013**, *15*, 15709–15726.
44. Zhang, L.; Yan, F.; Zhang, S. L.; Lei, D. S.; Charles, M. A.; Cavigiolio, G.; Oda, M.; Krauss, R. M.; Weisgraber, K. H.; Rye, K. A.; *et al*. Structural Basis of Transfer between Lipoproteins by Cholesteryl Ester Transfer Protein. *Nat. Chem. Biol.* **2012**, *8*, 342–349.
45. Zhang, L.; Song, J.; Cavigiolio, G.; Ishida, B. Y.; Zhang, S. L.; Kane, J. P.; Weisgraber, K. H.; Oda, M. N.; Rye, K. A.; Pownall, H. J.; *et al*. Morphology and Structure of Lipoproteins Revealed by an Optimized Negative-Staining Protocol of Electron Microscopy. *J. Lipid Res.* **2011**, *52*, 175–184.
46. Johnson, P. B.; Christy, R. W. Optical Constants of the Noble Metals. *Phys. Rev. Lett.* **1972**, *6*, 4370–4379.